

The Large Sky Area Multi-Object Fibre Spectroscopic Telescope (LAMOST) Quasar Survey: Quasar Properties from Data Release Two and Three

X. Y. Dong¹, Xue-Bing Wu^{1,2}, Y. L. Ai³, J. Y. Yang^{1,2}, Q. Yang^{1,2}, F. Wang^{1,2}, Y. X. Zhang⁴, A. L. Luo⁴, H. Xu^{1,2}, H. L. Yuan⁴, J. N. Zhang⁴, M. X. Wang⁴, L. L. Wang⁴, Y. B. Li⁴, F. Zuo⁴, W. Hou⁴, Y. X. Guo⁴, X. Kong⁴, X. Y. Chen⁴, Y. Wu⁴, H. F. Yang⁵, M. Yang⁶

sunne.xy.dong@pku.edu.cn

Received _____; accepted _____

¹Department of Astronomy, School of Physics, Peking University, Beijing, 100871, P.R. China

²Kavli Institute for Astronomy and Astrophysics, Peking University, Beijing, 100871, P.R. China

³School of Physics and Astronomy, Sun Yat-Sen University, Guangzhou 510275, China

⁴Key Laboratory of Optical Astronomy, National Astronomical Observatories, Chinese Academy of Sciences 100012, Beijing, China

⁵School of Computer Science and Technology, Taiyuan University of Science and Technology, Taiyuan 030024, China

⁶National Observatory of Athens, Vas. Pavlou & I. Metaxa, Penteli, 15236, Greece

ABSTRACT

This is the second installment for the Large Sky Area Multi-Object Fibre Spectroscopic Telescope (LAMOST) Quasar Survey, which includes quasars observed from September 2013 to June 2015. There are 9024 confirmed quasars in DR2 and 10911 in DR3. After cross-match with the SDSS quasar catalogs and NED, 12126 quasars are discovered independently. Among them 2225 quasars were released by SDSS DR12 QSO catalogue in 2014 after we finalised the survey candidates. 1801 sources were identified by SDSS DR14 as QSOs. The remaining 8100 quasars are considered as newly founded, and among them 6887 quasars can be given reliable emission line measurements and the estimated black hole masses. Quasars found in LAMOST are mostly located at low-to-moderate redshifts, with a mean value of 1.5. The highest redshift observed in DR2 and DR3 is 5. We applied emission line measurements to $H\alpha$, $H\beta$, $MgII$ and CIV . We deduced the monochromatic continuum luminosities using photometry data, and estimated the virial black hole masses for the newly discovered quasars. Results are compiled into a quasar catalog, which will be available online.

Subject headings: catalog - survey - quasars: general - quasars: emission lines

1. Introduction

Quasar is one of the most exotic celestial objects in the Universe. It emits a broad range of electromagnetic waves from γ -ray to radio (Antonucci 1993), and outshines its host galaxy by hundreds of times. Quasars can be used to trace the galaxy evolution (e.g. Schweitzer et al. 2006; Lutz et al. 2008; Bonfield et al. 2011; Dong & Wu 2016) and probe the intergalactic medium (e.g., Hennawi & Prochaska 2007; Huo et al. 2013, 2015).

There are many dedicated works to find more quasars ever since the first quasar was discovered by Schmidt (1963). Quasar’s unique spectral energy distribution, its high luminosity and variations are often used to select quasar survey candidates by separating them from normal galaxies and stars. By far, the most productive quasar survey is the Sloan Digital Sky Survey (SDSS; Schneider et al. 2010; Pâris et al. 2012, 2014). Another noticeable quasar survey is the Two-Degree Fields (2dF) Quasar Redshift Survey (Boyle et al. 2000). Both SDSS and 2dF use ultra-violet/optical photometric data to select their candidates. With the improvements of both quality and quantity of infrared surveys, optical/infrared photometric data provide another important tool to select quasar candidates (e.g., Wu & Jia 2010a; Wu et al. 2012; Ai et al. 2016). The extreme-deconvolution method with an optical-Infrared color cut is used by the SDSS-III’s Baryon Oscillation Spectroscopic Survey project (XDQSO; Bovy et al. 2011; Myers et al. 2015). Other data-mining and machine-learning algorithms are also adopted for quasar selection (e.g., Ross et al. 2012; Peng et al. 2012).

The Large Sky Area Multi-Object Fibre Spectroscopic Telescope (LAMOST) Quasar Survey is conducted under the LAMOST ExtraGalactic Survey (LEGAS; Zhao et al. 2012). Its quasar candidates are selected based on multi-color photometry and data-mining. The regular survey started in September 2012 and will be carried out through five to six years. This paper is the second installment in the series of LAMOST quasar survey, after

the pilot observations (Wu et al. 2010b,c) and data release 1 (Ai et al. 2016, Paper I). We will report LAMOST quasar survey data release two and three, which include quasars observed between September 2013 and June 2015. In section 2, we will briefly review the survey and candidate selections. Section 3 describes the visual inspections of the spectra. The emission line measurements and the black hole mass estimates are discussed in section 4 and 5. The parameters released with the quasar catalog are list in section 6. The last section is the summary. Throughout the paper, we adopt a Λ -dominated cosmology with $h = 0.7$, $\Omega_m=0.3$, and $\Omega_\Lambda =0.7$.

2. Survey outline

The Large Sky Area Multi-Object Fibre Spectroscopic Telescope (LAMOST), also known as Guoshoujing Telescope, is a 4-meter reflecting Schmidt telescope located at Xinglong Observatory, China (Cui et al. 2012; Zhao et al. 2012). It is equipped with 4000 fibres that across a 5° field of view. LAMOST has two sets of spectrographs. The blue channel covers spectrum from 3700\AA to 5900\AA , while the red channel covers spectrum from 5700\AA to 9000\AA . The spectral resolution R is about 1800 over the entire wavelength range.

2.1. Target selections

The potential quasars candidates are required to be point sources in SDSS image survey (Ahn et al. 2012) with a Galactic extinction corrected i -band Point Spread Function (PSF) magnitude brighter than 20mag. To avoid saturation and contamination from neighbour fibres, the magnitude upper-limit is set to be $i = 16$. The final candidates are selected from this candidate pool via two methods.

Optical-infrared colors. The foremost purpose of LEGAS quasar survey is to discover more quasars. Yet quasars at redshift 2 to 3 cannot be effectively identified in optical colour-colour space, because their colours are very similar to stars or galaxies (Schneider et al. 2010). Wu & Jia (2010a) and Wu et al. (2012) proposed to use optical-infrared color instead. In the LEGAS survey we adopted $Y - K > 0.46(g - z) + 0.82$ or $J - k > 0.45(i - Y - 0.366) + 0.64$ (Wu & Jia 2010a) for candidates with counterparts within the UKIDSS/Large Area Survey(LAS) DR8 (Lawrence et al. 2007), and $w1 - w2 > 0.57$ or $z - w1 > 0.66(g - z) + 2.01$ (Wu et al. 2012) for those found matches in WISE All-Sky Data Release (Wright et al. 2010). These selections mostly select quasars within redshift 4.

Data-mining algorithms. Some of the quasar candidates are selected using one of the following data-mining algorithms: support vector machine(SVM) classifiers (SVM; Peng et al. 2012), extreme deconvolution method (Bovy et al. 2011) and kernel density estimator (KDE; Richards et al. 2009).

There are also some supplemented candidates selected based on multi-wavelength (optical/X-ray/radio) matching, such as X-ray sources from ROSAT, XMM-Newton and Chandra, and radio sources from FIRST and NVSS. We included a group of SDSS DR7, DR9 and DR10 quasars on the purpose of testing LAMOST spectral liability. SDSS DR12 quasars are not removed because they were not released at the time when the candidate list was finalized for LAMOST. They are giving proper flags in the DR2 and DR3 quasar catalog. Some of our candidates overlap with the M31/M33 field (Huo et al. 2015). They are also flagged in the catalog.

2.2. Pipeline for data reduction

The details of LAMOST data reduction can be found in Luo et al. (2015). The raw data is reduced by the LAMOST 2D pipeline, which includes dark and bias removal, flat field correction, spectral extraction, sky subtraction and wavelength calibration. The output spectra are combinations of the blue and red channel spectra.

The LAMOST 1D pipeline provides spectral type classification and radial velocity (for stars) or redshift (for galaxies and quasars) using the cross-correlation method. The primary classifications given by LAMOST 1D pipeline are STAR, GALAXY, QSO, and UNKNOWN. In general QSO and UNKNOWN have fainter magnitudes, therefore, visual inspection is required to confirm their spectral type and assure the redshift measurement. In the next section, we will discuss the visual inspection and compare the results with the pipeline results.

3. Visual inspections of the spectra

As mentioned in the previous section, 1D pipeline results are not trustworthy for QSO and UNKNOWN types. A Java program ASERA (Yuan et al. 2013) is used to visually inspect each object with pipeline class QSO and quasar candidates with pipeline class UNKNOWN. The first step is to assure that the object is indeed a quasar. At the same time special objects such as BAL and disk emitter are labeled. In DR2, 9028 objects are identified as quasars, among them 2647 quasars are originally given UNKNOWN by the pipeline. Among 10911 confirmed DR3 quasars, 3428 quasars are previously UNKNOWN. There are still more than 12,000 quasar candidates with un-recognisable spectral type. They are returned to the candidates pool and will be re-observed in the future. The major reason to cause UNKNOWN type objects is the low S/N. It is either because the quasar candidates

with magnitudes close to $i = 20$ are difficult for LAMOST to obtain good spectra, or due to the poor observational conditions at the time. Figure 1 plots the distributions of the spectral S/N and the i -band PSF magnitude. It shows that the UNKONWN type spectra are fainter and have slightly lower S/N. If the blue and red channel spectra are improperly stacked, the combined spectrum might have artificial broad emission or absorption features, which also brings difficulties to pipeline classification.

The second step is to visually inspect redshift based on typical quasar emission lines, i.e., [OIII], MgII, CIII, and CIV. The poor quality of UNKNOWN type spectra also causes difficulties for pipeline to determine the redshift. For those with recognisable quasar emission lines, we visually estimate their redshifts using ASERA. But a flag will be given when there is only one emission line visualible. Sometimes, the visual inspected redshift mismatches the pipeline redshift. If there are at least two emission lines available, we manually correct the redshift, otherwise, we give a flag to indicate that the redshift for this object is arguable. Among visually confirmed quasars, 9484 have already been reported by SDSS. LAMOST pipeline gives redshifts of 6663 out of 9484, among them 95.7% has redshift difference less than 0.2. After visual inspection, another 2440 quasar redshifts are recovered, among them more than 98% have redshift differences less than 0.2 from SDSS. The redshifts of the remaining 381 SDSS-identified quasars cannot be measured using their LAMOST spectra of poor quality. Their redshift “Z_VI” in the catalog is 999 with Z_FLAG = 9. Figure 2 is the visual inspected redshift distributions of DR2 and DR3. The mean redshifts of DR2 and DR3 is 1.49 and 1.44, respectively. The quasar having the highest redshift in DR2 and DR3 is J132442.44+052438.8, with a redshift of 5.01. When $z \sim 1$, MgII locates at the overlapped wavelength ranges (around 6000Å) of the blue and red channels. If the spectral combinations of blue and red channels cause artificial features at the overlapping region, MgII might become unrecognisable. It explains the missing $z \sim 1$ objects in the distribution plots. Figure 3 plots DR2 and 3 quasars in the luminosity space,

where $M_i(z = 2)$ is K -corrected (Richards et al. 2006) absolute i -band PSF magnitude normalised to $z = 2$.

4. Spectral parameter measurements

In this section we describe the procedures of typical quasar emission line measurement. Detailed discussions please refer to Paper I.

Before the measurement, the LAMOST spectrum is corrected with Galactic extinction using the extinction map of Schlegel et al. (1998) and the reddening curve of Fitzpatrick (1999). Then the spectrum is shifted back to the rest frame.

Instead of fitting the continuum for the entire spectrum, we fit a local pseudo-continuum around each emission line (Shen et al. 2008). Two components are used for continuum fitting: a power law with its normalisation and slope as free parameters; and an FeII multiplet emissions with normalisation, velocity shift relative to the systemic redshift, and broadening velocity as free parameters. After subtraction of the local pseudo-continuum, the leftover of the spectrum is used for emission line fitting.

4.1. $H\alpha$

$H\alpha$ is only available when $z \leq 0.3$. The regions used for pseudo-continuum fitting are 6000-6250Å and 6800-7000Å. The template of optical FeII emission is from Véron-Cetty et al. (2004). $H\alpha$ is modelled with one narrow and one broad component. The broad component is fitted with as many Gaussians as statistically justifiable (the typical number of Gaussian is four, see Dong et al. (2008) for detailed discussion). The narrow component is fitted with a single Gaussian with an upper limit of the full width half-maximum

(FWHM) of 1200 km s^{-1} . The velocity offsets and line widths of $[\text{NII}]\lambda\lambda 6548, 6584$ and $[\text{SII}]\lambda\lambda 6717, 6731$ are tied to $\text{H}\alpha$ narrow component. The relative flux ratio of the two $[\text{NII}]$ components is fixed to 2.96. Figure 4 gives an example of $\text{H}\alpha$ fit.

4.2. $\text{H}\beta$

When $z \leq 0.75$, $\text{H}\beta$ is available. The regions for pseudo-continuum fitting are $4435\text{-}4700\text{\AA}$ and $5100\text{-}5535\text{\AA}$. The template of optical FeII emission is from Véron-Cetty et al. (2004). $\text{H}\beta$ is also modelled with a narrow and a broad component. The broad component is fitted with as many Gaussians as statistically justifiable (Dong et al. 2008). The narrow component is fitted with a single Gaussian with an upper limit of $\text{FWHM} = 1200 \text{ km s}^{-1}$. For each line of the $[\text{OIII}]\lambda\lambda 4959, 5007$ doublet, two Gaussians are used: one for the core and the other for a possible blue wing. The doublet are assumed to have same redshifts and profiles, with their flux ratio fixed to 3. The velocity offsets and line widths of the doublet core components are tied to $\text{H}\beta$ narrow component. Figure 5 gives an example of $\text{H}\beta$ fit.

4.3. MgII

MgII is measured when quasar redshift is between 0.40 and 1.76. The pseudo-continuum is fitted using data from $2200\text{-}2700 \text{\AA}$ and $2900\text{-}3090\text{\AA}$. An ultraviolet FeII template from Tsuzuki et al. (2006) is included in the continuum fitting. One narrow component and one broad component are used to fit each of the $\text{MgII}\lambda\lambda 2796, 2803$ doublet. The narrow component is a single Gaussian with a FWHM less than 900 km s^{-1} . The broad component is a truncated five-parameter Gauss-Hermite series. The broad component of each MgII doublet line is assumed to have same profile with flux ratio set to be between 2:1 and 1:1

(Laor et al. 1997). The same assumption is applied to the narrow component of each MgII doublet line. Figure 6 shows an example of MgII fit.

4.4. CIV

CIV is measured when quasar redshift is larger than 1.58. The fitting regions for the pseudo-continuum are 1145-1465Å and 1700-1705Å. One Gaussian and one Gaussian-Hermite are used to fit CIV emission. There is no upper limit set for the FWHM of the Gaussian function, because the existence of a strong narrow component for CIV is still debatable. An example of CIV fitting is presented in Figure 7.

The distributions of the FWHM of H α , H β , MgII, and CIV are shown in Figure 8. After spectra measurements, each fitting results are inspected visually. Flags are added based on the quality of the fit.

4.5. The reliability of the emission line fitting.

As mentioned in Paper I, the core routines of the emission line fitting are adopted from Dong et al. (2008) and Wang et al. (2009), which used the MPFIT package (Markwardt 2009) to perform χ^2 -minimization using the Levenberg-Marquardt technique. One may find the detailed discussion of the measurement uncertainties and justifications in Dong et al. (2008, Section 2.5) and Wang et al. (2009, Section 2.2). Shen et al. (2011, Section 3.3, thereafter Shen11) also provides a detailed discussion regarding the different measurements of MgII. To justify the fitting results of this set of data, we provide the simple comparisons between LAMOST DR2&3 and that of Shen11. Histograms on the left side of Figure 9 compare the FWHMs of H β , MgII, and CIV, while histograms on the right side compare their EWs. It appears that our measurements of FWHM and EW for H β and CIV are

smaller than Shen11, with a mean difference of -0.079 ± 0.19 dex and -0.16 ± 0.21 dex for $H\beta$, and -0.043 ± 0.35 dex and -0.10 ± 1.6 . The FWHM of MgII is larger than Shen11 and the EW is smaller, with a mean difference of 0.048 ± 0.18 dex and -0.061 ± 0.28 dex respectively. As mentioned in previous sections, four Gaussians are used to fit the broad component of $H\beta$, and one Gaussian and one Gaussian-Hermite functions are used to fit the CIV emission line in our work. In Shen11 a single or a maximum number of three Gaussians are used to fit the broad component of $H\beta$ and CIV. For MgII, we used doublets with one narrow and one broad components, while Shen11 used one or a maximum number of three Gaussians. Shen11 states that these two fitting procedures yield consistent results in FWHM of MgII after applying both methods on the SDSS spectra. It is plausible that the small differences showed in Figure 9 are due to the differences in the fitting procedures and/or the different SNRs of LAMOST/SDSS spectra.

5. Continuum luminosity and the virial black hole mass

The LAMOST survey is not equipped with a photometry telescope (Song et al. 2012). Its large field of view makes it difficult in some cases to find a suitable flux standard star for each spectrograph especially for those relatively faint extra-galactic objects. Therefore, the released LAMOST quasar spectra either are not flux calibrated or have poor flux calibrations. To estimate continuum luminosity we use the five-band SDSS photometry instead. The PSF magnitudes of each quasar are retrieved from SDSS photometry database. Before the photometry fit, these magnitudes are corrected with Galactic extinction and converted to flux density, F_λ , where λ is the effective wavelength of each filter. Two components are used to fit the photometry, i.e., a continuum spectrum and an emission line template. As described in Vanden Berk et al. (2001)(hereafter VB01), the continuum spectrum can be represented by two power-laws with a break at 4661\AA . The spectral indices

given by VB01 are $\alpha_\lambda = -1.54$ at the blueward of 4661\AA and $\alpha_\lambda = -0.42$ at the redward of 4661\AA . The emission line template is generated by removing the continuum spectrum from the composite median quasar spectrum. The normalisations of the continuum spectrum and emission line template are free parameters. The other two free parameters are the spectral indices of the two power-laws, with $\alpha_\lambda = -1.54$ and $\alpha_\lambda = -0.42$ as their initial values, respectively. The fitting uses Python PYTOOLS.NMPFIT ¹ to perform χ^2 -minimization with the Levenberg-Marquardt algorithm. Figure 10 presents two luminosity fitting examples. The results are well matched with the composite spectrum (Vanden Berk et al. 2001), with an average spectral index of -1.52 blueward of 4661\AA and -0.33 redward of 4661\AA . The monochromatic continuum luminosities at 1350\AA , 3000\AA , and 5000\AA are calculated from the power-law continuum spectra. We compared the monochromatic continuum luminosities to Shen et al. (2011) and drew the histograms on the left side of Figure 11. It is clear that our results agree very well with Shen et al. (2011).

We calculate virial black hole mass using $H\beta$, $MgII$ and CIV based on Shen et al. (2011) scheme as follows:

- $M_{BH}(H\beta)$,

$$\text{Log}_{10}\left(\frac{M_{BH, \text{vir}}}{M_\odot}\right) = 0.910 + 0.50\text{Log}_{10}\left(\frac{L_{5100}}{10^{44}\text{erg s}^{-1}}\right) + 2\text{Log}_{10}\left(\frac{\text{FWHM}(H\beta)}{\text{km s}^{-1}}\right) \quad (1)$$

(Vestergaard & Peterson 2006)

- $M_{BH}(MgII)$,

$$\text{Log}_{10}\left(\frac{M_{BH, \text{vir}}}{M_\odot}\right) = 0.740 + 0.62\text{Log}_{10}\left(\frac{L_{3000}}{10^{44}\text{erg s}^{-1}}\right) + 2\text{Log}_{10}\left(\frac{\text{FWHM}(MgII)}{\text{km s}^{-1}}\right) \quad (2)$$

(Vestergaard & Osmer 2009)

¹<http://cars.uchicago.edu/software/python/index.html>

- $M_{\text{BH}}(\text{CIV})$,

$$\text{Log}_{10}\left(\frac{M_{\text{BH,vir}}}{M_{\odot}}\right) = 0.660 + 0.53\text{Log}_{10}\left(\frac{L_{1350}}{10^{44}\text{erg s}^{-1}}\right) + 2\text{Log}_{10}\left(\frac{\text{FWHM}(\text{CIV})}{\text{km s}^{-1}}\right) \quad (3)$$

(Shen & Kelly 2010).

In principle, the virial black hole mass should be estimated using single-epoch spectra, which is not possible for LAMOST quasars. Because the time difference between SDSS photometry and the LAMOST observation, the variations of quasar luminosity might be 0.1-0.2 mag (Vanden Berk et al. 2004; Zuo et al. 2012; Ai et al. 2013). We compared our estimated BH masses to Shen et al. (2011) and show the results on the right side of Figure 11. In average, LAMOST DR2&3 $H\beta$ estimated BH mass is 0.23 ± 0.37 dex smaller than Shen et al. (2011), the MgII estimated BH mass is 0.12 ± 0.38 dex smaller, and the CIV estimated BH mass is 0.020 ± 0.35 dex smaller. Comparing to the FWHM differences in Figure 9, the difference between BH mass estimate is mostly due to the difference between the FWHM measurements. We drew the BH mass distributions of LAMOST DR2&3 and Shen et al. (2011) along the redshift in Figure 12. It is clear that even with a slightly different BH mass estimate, the LAMOST quasars still occupy the same BH mass space as Shen et al. (2011). The BH mass given in this work can be considered as a good approximation.

6. Catalog parameters

We provide a compiled catalog for all quasars observed in LAMOST DR2 and DR3. Parameters included in the quasar catalog is list in Table 2. Below we describe each parameter in details.

1. OBSID: unique object identification in LAMOST database.

2. Designation: LAMOST Jhhmmss.s+ddmmss.s (J2000)

3-4. Right ascension and Declination

5-8: Spectral observation information. MJD: modified Julian data; PLANID: spectroscopic plan identification; SPID: spectrograph identification; FIBERID: fibre number. A LAMOST spectrum is named as *spec-MJD-PLANID-SPID-FIBERID.fits*

9: SOURCE_FLAG: SOURCE_FLAG is a 7-bit binary digit. The first three bits indicate whether the quasar is already reported by SDSS or NED (i.e., “011” in SDSS DR7, DR9 or DR10, “001” in DR12, “100” reported in DR14, “010” reported in NED but not in SDSS, and “000” neither reported by SDSS nor NED). The two bits in the middle indicate how the quasar candidate is selected (i.e., “00” infrared-optical colour selected, “01” data mining selected, “10” object not included in LAMOST LEGAS quasar survey sample but identified as quasar). The last two bits indicate whether the quasar is overlapped with M31/M33 field (“00” not overlapped, “01” object already reported in Huo et al. (2015), “10” object in M31/M33 field but not in Huo et al. (2015)). For example SOURCE_FLAG=64. “64” written in binary system is “1000000”. It means the quasar has already been reported by DR14, it was selected via infrared-optical colour selection, and is not within M31/M33 field.

10: M_i . Absolute i band magnitude with K -correction to $z = 2$ following Richards et al. (2006)

11-12: CLASS_VI and CLASS_FLAG. Visually inspected spectral type. If the spectral type is uncertain CLASS_FLAG = 1.

13-15: Redshift. Z_PIPELINE: redshift given by LAMOST pipeline; Z_VI: redshift confirmed by visual inspection. If the value of redshift is uncertain (e.g., only one emission line available), Z_FLAG=1. If the spectrum is likely a quasar but too noisy to yield a

redshift, Z_FLAG=9.

16: SNR_SPEC. Median S/N per pixel in the wavelength regions of 4000-5700Å and 6200-9000Å.

17-23: FWHM and the rest-frame equivalent width of H α , [NII]6584, and [SII] $\lambda\lambda$ 6718, 6732

24: Rest-frame equivalent width of iron emission at 6000-6500Å.

25-26: Number of good pixels and median S/N per pixel for the H α region in 6400-6755 Å.

27: LINE_REDCHI2_HA. Reduced χ^2 of H α emission line fit.

28: LINE_FLAG_HA. Flag indicates the quality of H α fitting. As mentioned in Section 4.5, the MPFIT package (Markwardt 2009) is used to perform χ^2 -minimization using the Levenberg-Marquardt technique. The fitting automatically assigns “0” to those with converged results and “-1” without converged results. The un-converged fits are usually caused by low S/N, too few good pixels in the fitting region, or peculiar continuum and emission line properties. After fitting, we visually inspect each fitting result with LINE_FLAG_HA=0. For those with clearly over-subtracted continuum we changed their flag from 0 to 1 to flag an unreliable fit. If H α is outside the observational frame, LINE_FLAG_HA=-1.

29-34: FWHM and the rest-frame equivalent width of H β and [OIII] $\lambda\lambda$ 4959, 5007.

35: Rest-frame equivalent width of iron emission at 4435-4685 Å

36-37: Number of good pixels and median S/N per pixel for the H β region in 6400-6755 Å.

38: LINE_REDCHI2_HB. Reduced χ^2 of H β emission line fit.

39: LINE_FLAG_HB. Quality flag for H β fitting. It is defined using the same scheme as LINE_FLAG_HA.

40-48: FWHM and the rest-frame equivalent width of MgII.

49-50: Number of good pixels and median S/N per pixel for MgII.

51: LINE_REDCHI2_MG. Reduced χ^2 of MgII emission line fit.

52: LINE_FLAG_MG. Quality flag for MgII fitting. It is defined using the same scheme as LINE_FLAG_HA.

53-58: FWHM and the rest-frame equivalent width for CIV.

59-60: Number of good pixels and median S/N per pixel for CIV.

61: LINE_REDCHI2_CIV. Reduced χ^2 of CIV emission line fit.

62: LINE_FLAG_CIV. Quality flag for CIV fitting. It is defined using the same scheme as LINE_FLAG_HA. For those BAL candidates, values of LINE_FLAG_CIV are also changed to 1.

63: ALPHA1. Continuum spectral index α_λ , where $1300 < \lambda < 4661\text{\AA}$

64: ALPHA2. Continuum spectral index α_λ , where $\lambda > 4661\text{\AA}$

65: MODEL_PHOT_CHI2. Reduced χ^2 of continuum fit.

66: CONT_FLAG. Continuum fitting flag. As mentioned in Section 5, Python PYTOOLS.NMPFIT is used to perform χ^2 -minimization with the Levenberg-Marquardt algorithm. When the fitting converges, CONT_FLAG=0. If the fitting cannot converge, CONT_FLAG=1. The un-converged fitting usually happens when the SDSS 5-band magnitudes form a peculiar shape, therefore, cannot be fitted with the composite spectrum.

67-72: Monochromatic luminosity calculated from the break power-law continuum.

The relative errors are calculated via Monte-Carlo simulation.

73-81: Virial BH mass, error and flags. The BH mass error are calculated using Monte-Carlo simulation. Since BH mass is estimated using FWHM and monochromatic continuum luminosity, the flags of the BH mass are the combinations of the emission line fitting flags and the continuum fitting flags as shown in Table 1. When the LOGMBH_FLAG = -1, there is no available BH mass estimate. If the LOGMBH_FLAG = 1, the BH mass estimate should be used with caution.

Table 1:: The determination of BH mass flags.

LOGMBH_FLAG		CONT_FLAG	
		1	0
LINE_FLAG	-1	-1	-1
	1	-1	1
	0	-1	0

7. Summary

In this work, we present LAMOST LEGAS Quasar Survey Data Release Two and Three. There are 9024 confirmed quasars in DR2 and 10911 in DR3. Among them 8100 quasars are not reported in either SDSS or NED. As mentioned before, our survey candidates were finalised before SDSS DR12, therefore 2225 SDSS DR12 QSO catalogue released quasars and 1810 DR14 QSOs should also be considered as independent discovery. The bottom two pie plots in Figure 13 show the sources of the quasar candidates. In DR2, 44.8% quasars are from infrared-optical color selection, 41.4% are from data-mining, the remaining 13.8% are quasars that were not submitted as quasar candidates initially. In

DR3, 52.0% quasars are from infrared-optical color selection, 44.0% are from data-mining, the remaining 4% are not quasar candidates but are confirmed as quasars. It indicates that infrared-optical color selection is a promising method for selecting quasars. The top two pie plots are the cross-matching results between LAMOST quasar and SDSS quasar. In both DR2 and DR3, about 50% of LAMOST quasars are not reported by SDSS. It shows that LAMOST quasars provide a great supplement to low-to-moderate redshift quasars.

For each confirmed quasar, we applied emission line measurements of $H\alpha$, $H\beta$, $MgII$ and CIV . We conducted a continuum fit using SDSS photometry data. We also estimated the black hole mass for each quasar. The results are compiled into one quasar catalog. Proper flags are added to indicate the liability of the fit or the estimate. Both LAMOST quasar spectra and the quasar catalog are available on-line. Follow-up studies based on LAMOST Quasar Survey, such as BAL study, are under way.

Acknowledgements

We acknowledge the support from the National Key Basic Research Program of China (grant 2014CB845700), the Ministry of Science and Technology of China under grant 2016YFA0400703, NSFC grants 11373008 and 11533001, and the Strategic Priority Research Program "The Emergence of Cosmological Structures Grant No. XDB09000000) of National Astronomical Observatories, Chinese Academy of Sciences. The Guo Shou Jing Telescope (the Large Sky Area Multi-Object Fiber Spectroscopic Telescope, LAMOST) is a National Major Scientific Project built by the Chinese Academy of Sciences. Funding for the project has been provided by the National Development and Reform Commission. LAMOST is operated and managed by National Astronomical Observatories, Chinese Academy of Sciences.

REFERENCES

- Ahn, C. P., Alenandroff, R., Rachael, A. P., et al. 2012, *ApJS*, 203, 21
- Ai, Y. L., Yuan, W., Zhou, H., et al. 2013, *AJ*, 145, 90
- Ai, Y. L., Wu, X.-B., Yang, J. Y., et al. 2016, *AJ*, 151, 24
- Antonucci, R., 1993, *ARA&A*, 31, 473
- Bonfield, D. G., Jarvis, M. J., Hardcastle, M. J., et al. 2011, *MNRAS*, 416, 13
- Bovy, J., Hennawi, J. F., Hogg, D. W., et al. 2011, *ApJ*, 729, 141
- Boyle, B. J., Shanks, T., Croom, S. M., et al. 2000, *MNRAS*, 317, 1014
- Cui, X. Q., Zhao, Y. H., Chu, Y. Q., et al. 2012, *Research in Astronomy and Astrophysics*, 12, 1197
- Dong, X.-B., Wang, T.-G., Wang, J.-G., et al. 2008, *MNRAS*, 383, 581
- Dong, X. Y., Wu, X.-B. 2016, *ApJ*, 824, 70
- Fitzpatrick, E. L. 1999, *PASP*, 111, 63
- Hennawi, J. F., Prochaska, J. X. 2007, *ApJ*, 655, 735
- Huo, Z. Y., Liu, X. W., Xiang, M. S., et al. 2013, *AJ*, 145, 159
- Huo, Z. Y., Liu, X. W., Xiang, M. S., et al. 2015, *Research in Astronomy and Astrophysics*, 15, 1438
- Lawrence, A., Warren, S. J., Almaini, O., et al. 2007, *MNRAS*, 379, 1599
- Laor, A., Jannuzi, B. T., Gree, R. F., & Boroson, T. A. 1997, *ApJ*, 489, 656

- Luo, A.L., Zhao, Y. H., Zhao, G., et al. 2015, *Research in Astronomy and Astrophysics*, 15, 1095
- Lutz, D., Sturm, E., Tacconi, L. J., et al. 2008, *ApJ*, 684, 853
- Markwardt, C. B. 2009, *ASP Conf. Ser. 411, Astronomical Data Analysis Software and Systems XVIII*, ed. D. A. Bohlender, D. Daniel, & P. Dowler (San Francisco, CA: ASP), 251
- Myers, A. D., Palanque-Delabrouille, N., Prakash, A., et al. 2015, *ApJS*, 221, 27
- Pâris, I., Petitjean, P., Aubourg, É., et al. 2012, *A&A*, 548, A66
- Pâris, I., Petitjean, P., Aubourg, É., et al. 2014, *A&A*, 563, A54
- Peng, N.B., Zhang, Y. X., Zhao, Y. H., & Wu, X.-B. 2012, *MNRAS*, 425, 2599
- Richards, G. T., Strauss, M. A., Fan, X., et al. 2006, *AJ*, 131, 2766
- Richards, G. T., Myers, A. D., Gray, A.G., et al. 2009, *ApJS*, 180, 67
- Ross, N. P., Myers, A. D., Sheldon, E. S., et al. 2012, *ApJS*, 199, 3
- Schlegel, D. J., Finkbeiner, D. P. & Davis, M. 1998, *ApJ*, 500, 525
- Schmidt, M., 1963, *Nature*, 197, 1040
- Schneider, D. P., Richards, G. T., Hall, P. B., et al. 2010, *AJ*, 139, 2360
- Schweitzer, M., Lutz, D., Sturm, E., et al. 2006, *ApJ*, 649, 79
- Shen, Y., Greene, J. E., Strauss, M. A., et al. 2008, *ApJ*, 680, 169
- Shen, Y. & Kelly, B. C. 2010, *ApJ*, 713, 41
- Shen, Y., Richards, G. T., Strauss, M. A., et al. 2011, *ApJS*, 194, 45

- Song, Y. H., Luo, A. L., Comte, G., et al. 2012, *Research in Astronomy and Astrophysics*, 12, 453
- Tsuzuki, Y., Kawara, K., Yoshii, Y., et al. 2006, *ApJ*, 650, 57
- Vanden Berk, D. E., Richards, G. T., Bauer, A., et al. 2001, *AJ*, 122, 549
- Vanden Berk, D. E., Wilhite, B. C., Kron, R. G., et al. 2004, *ApJ*, 601, 692
- Véron-Cetty, M.-P., Joly, M., Véron, P. 2004, *A&A*, 417, 515
- Vestergaard, M. & Peterson, B. M. 2006, *ApJ*, 641, 689
- Vestergaard, M. & Osmer, P. S. 2009, *ApJ*, 699, 800
- Wang, J.-G., Dong, X.-B., Wang, T.-G., et al. 2009, *ApJ*, 707, 1334
- Wright, E. L., Eisenhardt, P. R. M., Mainzer, A. K., et al. 2010, *AJ*, 140, 1868
- Wu, X.-B., Jia, Z. 2010, *MNRAS*, 406, 1583
- Wu, X.-B., Chen, Z.-Y., Jia, Z.-D., et al. 2010, *Research in Astronomy and Astrophysics*, 10, 737
- Wu, X.-B., Jia, Z.-D., Chen, Z.-Y., et al. 2010, *Research in Astronomy and Astrophysics*, 10, 745
- Wu, X.-B., Hao, G., Jia, Z., et al. 2012, *AJ*, 144, 49
- Yuan, H.L., Zhang, H.T., Zhang, Y. X., et al. 2013, *A&C*, 3, 65
- Zhao, G., Zhao, Y. H., Chu, Y. Q., et al. 2012, *Research in Astronomy and Astrophysics*, 12, 723
- Zuo, W. W., Wu, X.-B., Liu, Y. Q., Jiao, C. L. 2012, *ApJ*, 758, 104

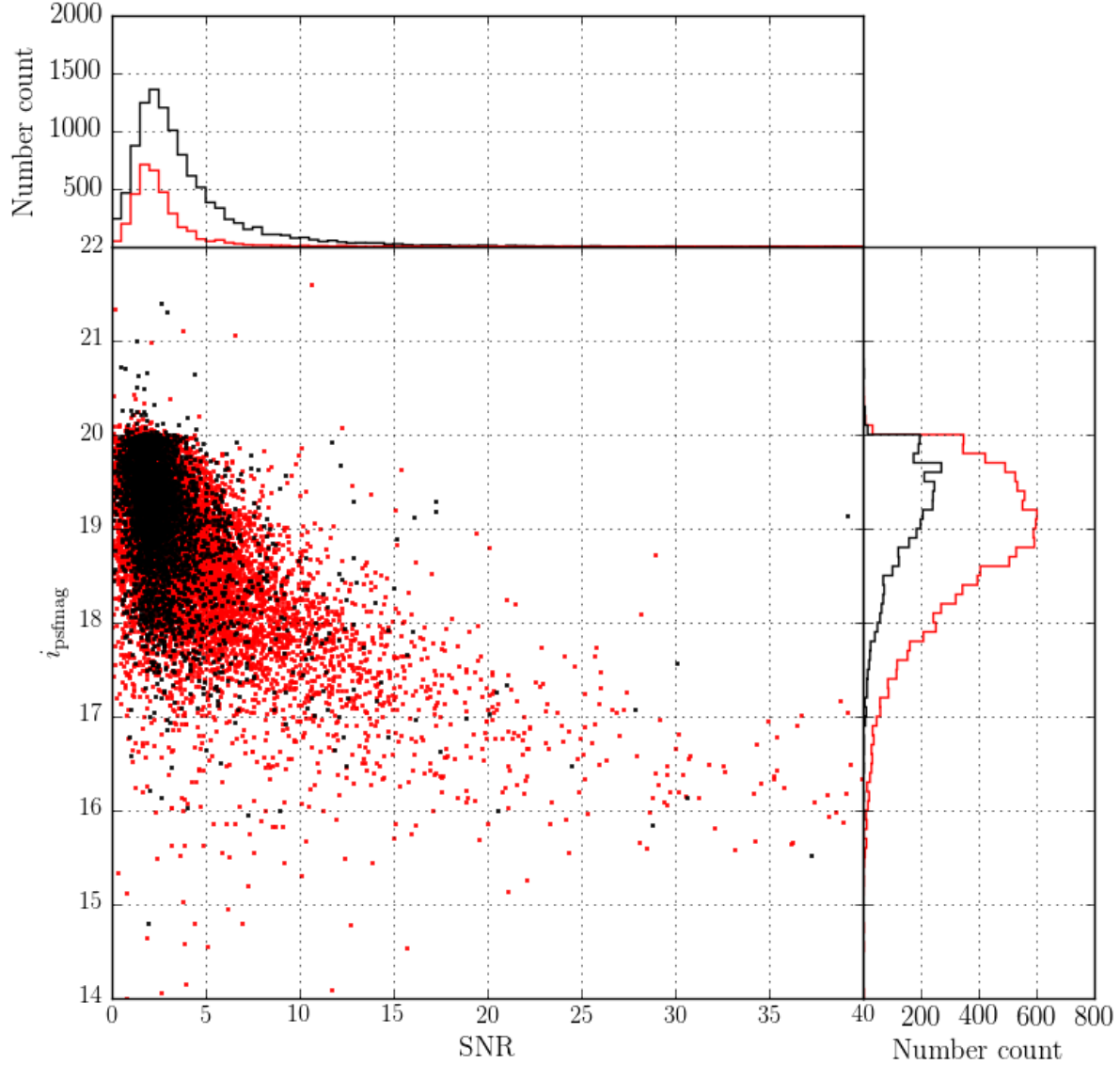


Fig. 1.— i -band PSF magnitude and the S/N of the spectrum. Red dots are pipeline QSOs. Black dots are pipeline UNKNOWNs but visually identified as quasars. The mean S/N of pipeline QSOs is 4.2, higher than the value of UNKNOWNs which is 2.8. The mean i -band magnitude of pipeline QSOs is 18.8 slight brighter than the UNKNOWNs’ 19.1.

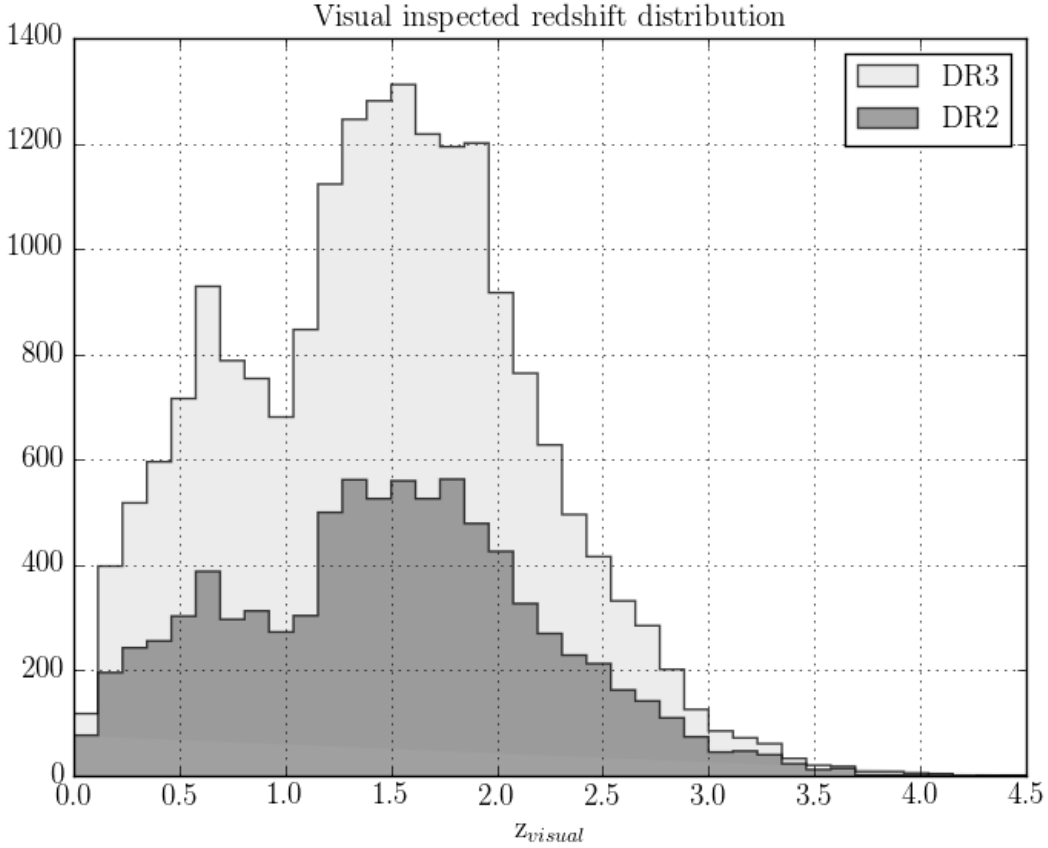


Fig. 2.— The visual inspected redshift distributions of DR2 (dark-grey) and DR3 (light-grey) quasars. The mean redshifts are 1.49 for DR2 and 1.43 for DR3, respectively. The quasar having highest redshift in DR2 is J132442.44+052438.8, with $z = 5.01$. The quasar having highest redshift in DR3 is J112811.44+302255.9, with $z = 4.90$. There are clear gaps in both DR2 and DR3 around $z \sim 1$. It is mostly due to the artificial features at the spectral stacking region.

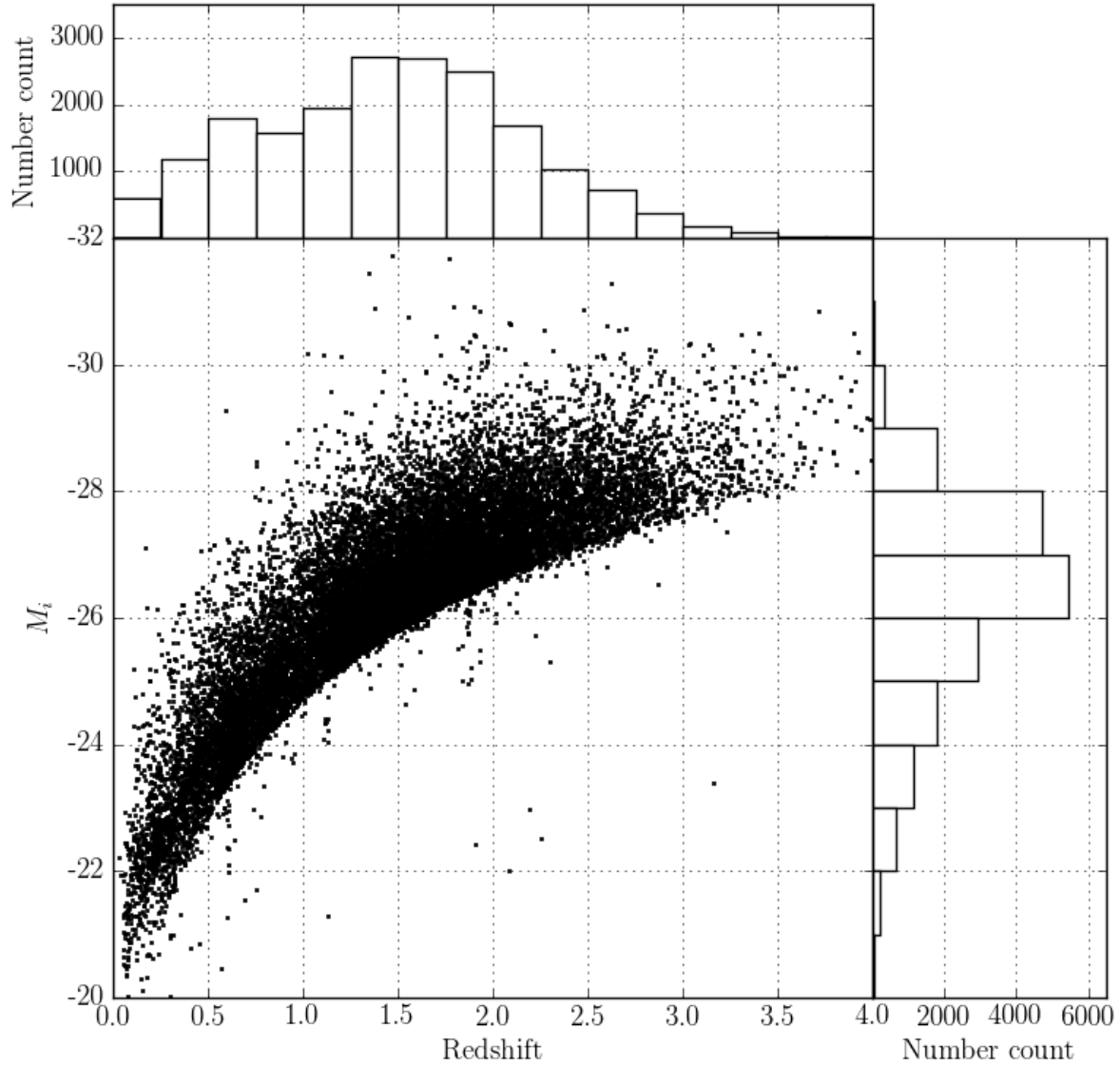


Fig. 3.— The redshift distribution on the luminosity space. The y-axis is the absolute i band PSF magnitude with the Galactic extinction correction. The K -correction is normalised to $z = 2$, following Richards et al. (2006).

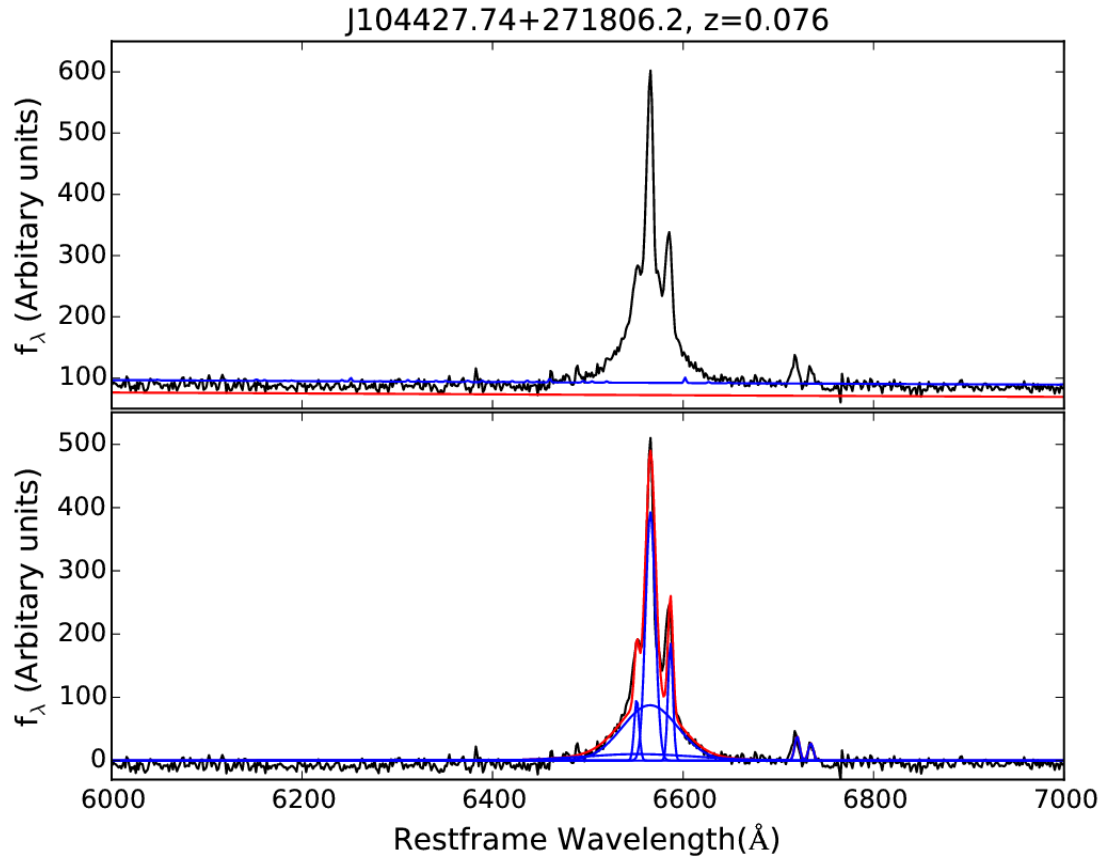


Fig. 4.— Example of H α measurement for J104427.74+271806.2, $z = 0.076$. The top panel shows the pseudo-continuum fit. The red line is the power-law, the blue line is the power-law plus FeII template. The bottom panel shows the H α emission line and [NII] fitting. The black line is the continuum subtracted spectrum. Each blue line represents one component. The red line is the combined emission line profile.

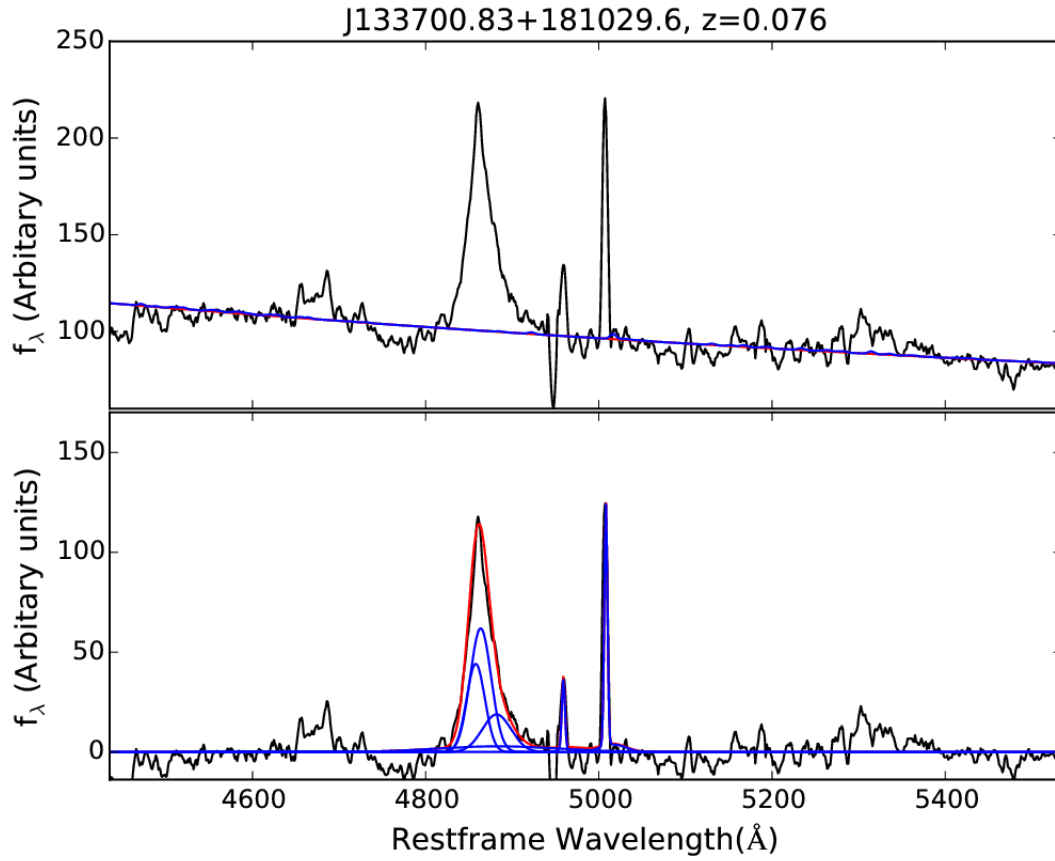


Fig. 5.— Example of $H\beta$ measurement for J133700.83+181029.6, $z = 0.076$. The top panel shows the pseudo-continuum fit. The red line is the power-law, the blue line is the power-law plus FeII template. The bottom panel shows the $H\beta$ emission line and [OIII]. The black line is the continuum subtracted spectrum. Each blue line represents one component. The red line is the combined emission line profile.

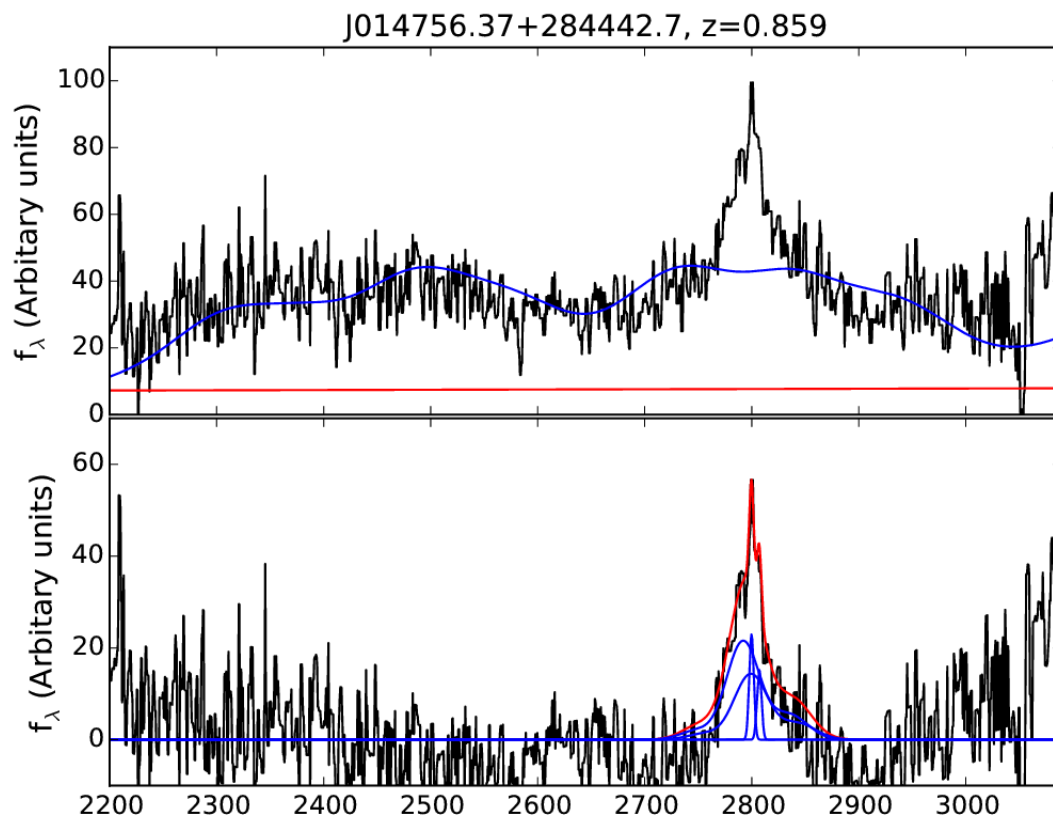


Fig. 6.— MgII measurement for J014756.37+284442.7, $z = 0.859$. The top panel shows the pseudo-continuum fit. The red line is the power-law, the blue line is the power-law plus FeII template. The bottom panel shows MgII doublet fit. The black line is the continuum subtracted spectrum. The blue lines include one narrow and one broad components for each of the MgII doublet. The red line is the combined MgII profile.

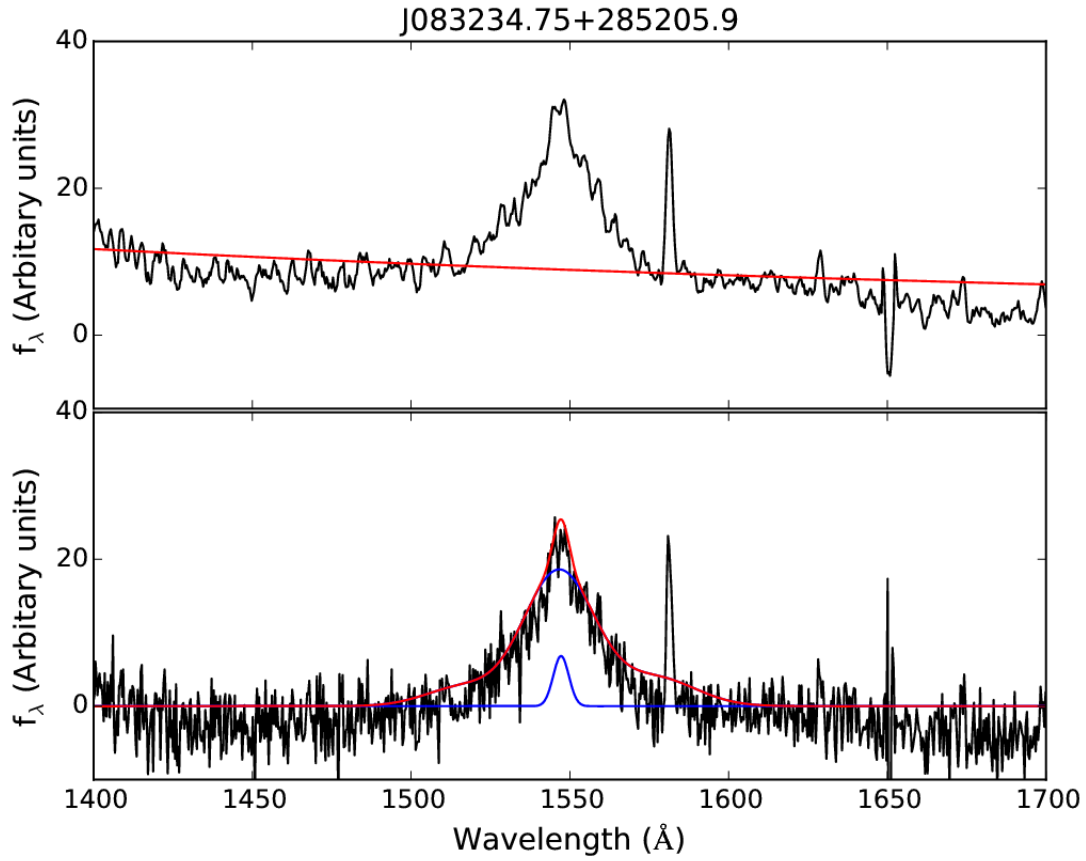


Fig. 7.— CIV measurement for J083234.75+285205.9, $z = 2.34$. The top panel shows the pseudo-continuum fit. The red line is the power-law. The bottom panel shows the CIV emission line measurement. The black line is the continuum subtracted spectrum. One of the blue line is a single Gaussian, the other blue line is a Gaussian-Hermite series. The red line is the combined emission line profile.

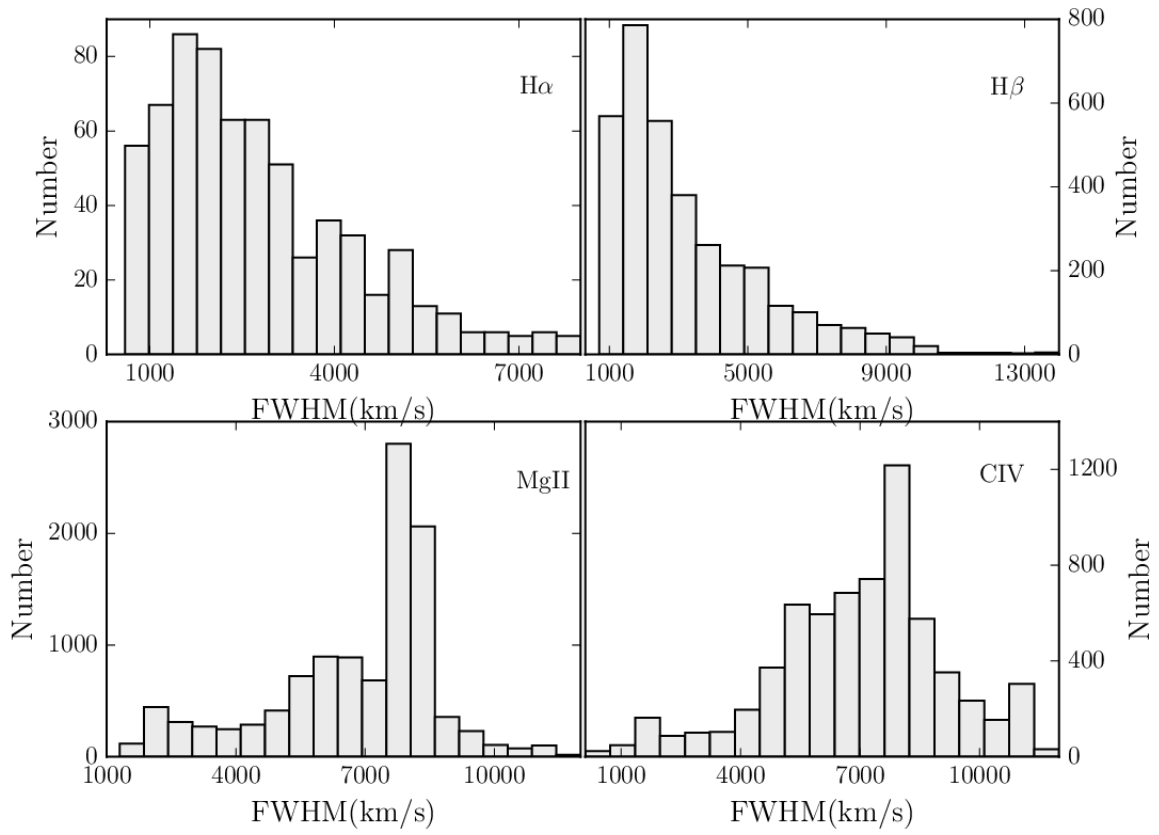


Fig. 8.— The distributions of FWHM of emission lines H α , H β , MgII, and CIV.

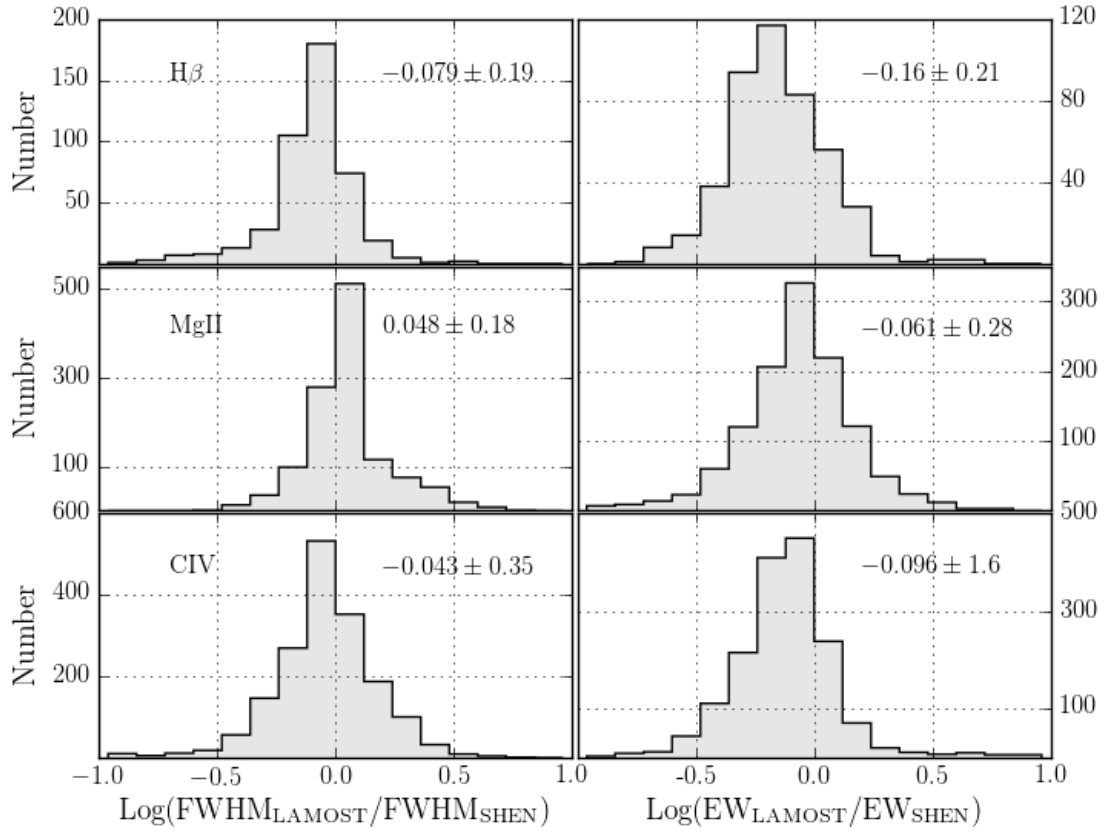


Fig. 9.— The comparisons of FWHM and EW between LAMOST DR2&3 and Shen et al. (2011).

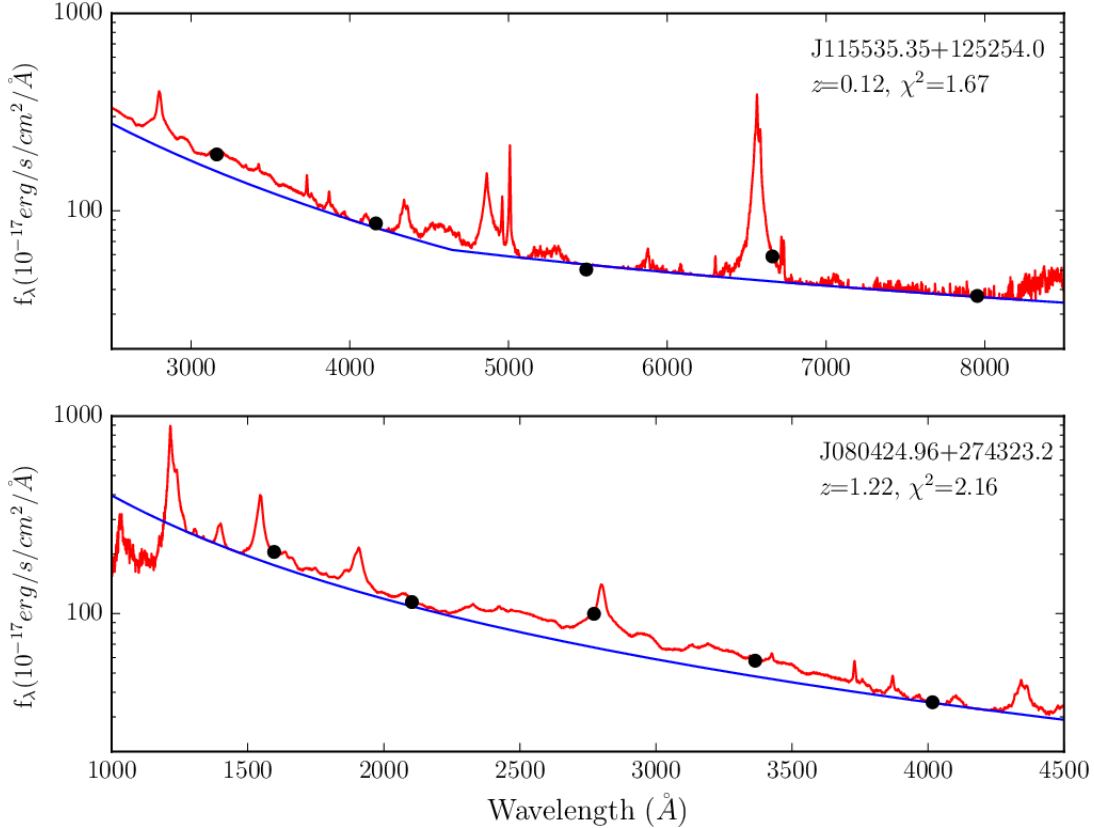


Fig. 10.— Two examples of continuum fitting. The x-axis is the rest-frame wavelength, the y-axis is the flux density. The black dots are 5-band SDSS photometry. The blue lines are the continuum represented by two power-laws. The red lines are composite spectra. The top panel is a quasar with $z = 0.12$, its continuum has a clear break at 4661 \AA . The bottom panel is a quasar with $z = 1.22$, a single power-law is required for its continuum.

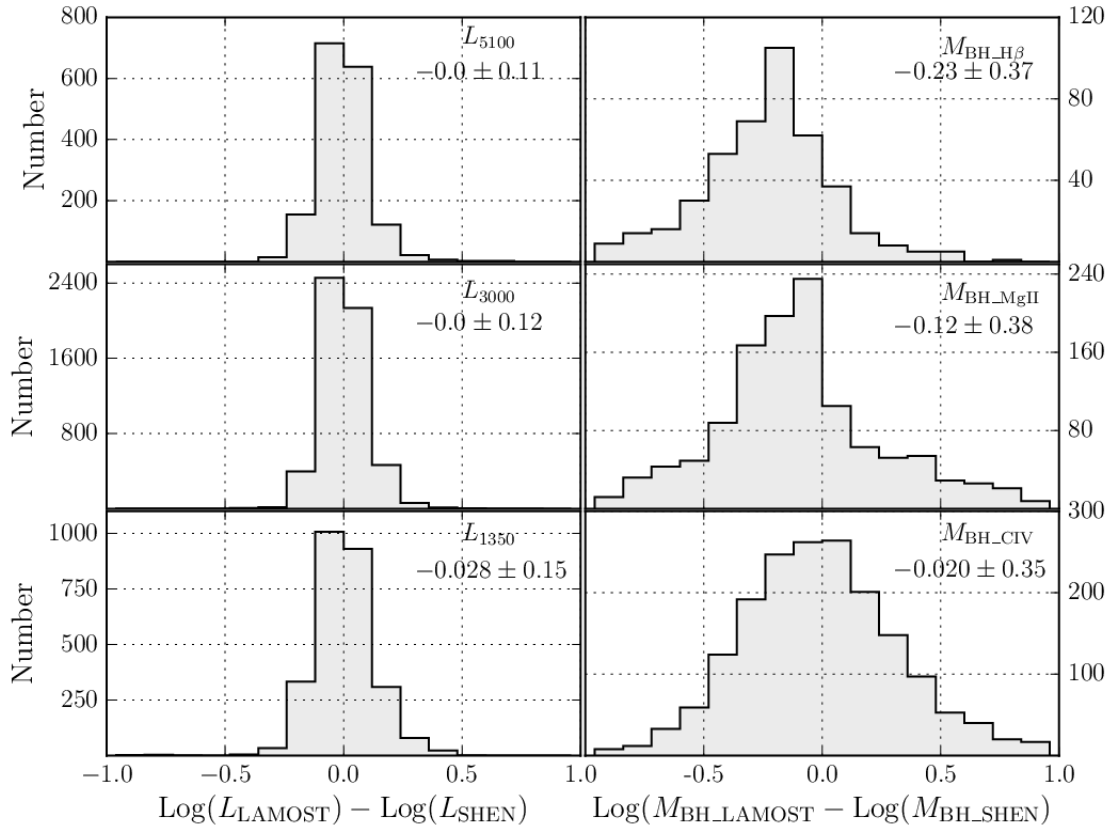


Fig. 11.— The comparisons of the monochromatic continuum luminosities and the estimated BH masses with those in Shen et al. (2011).

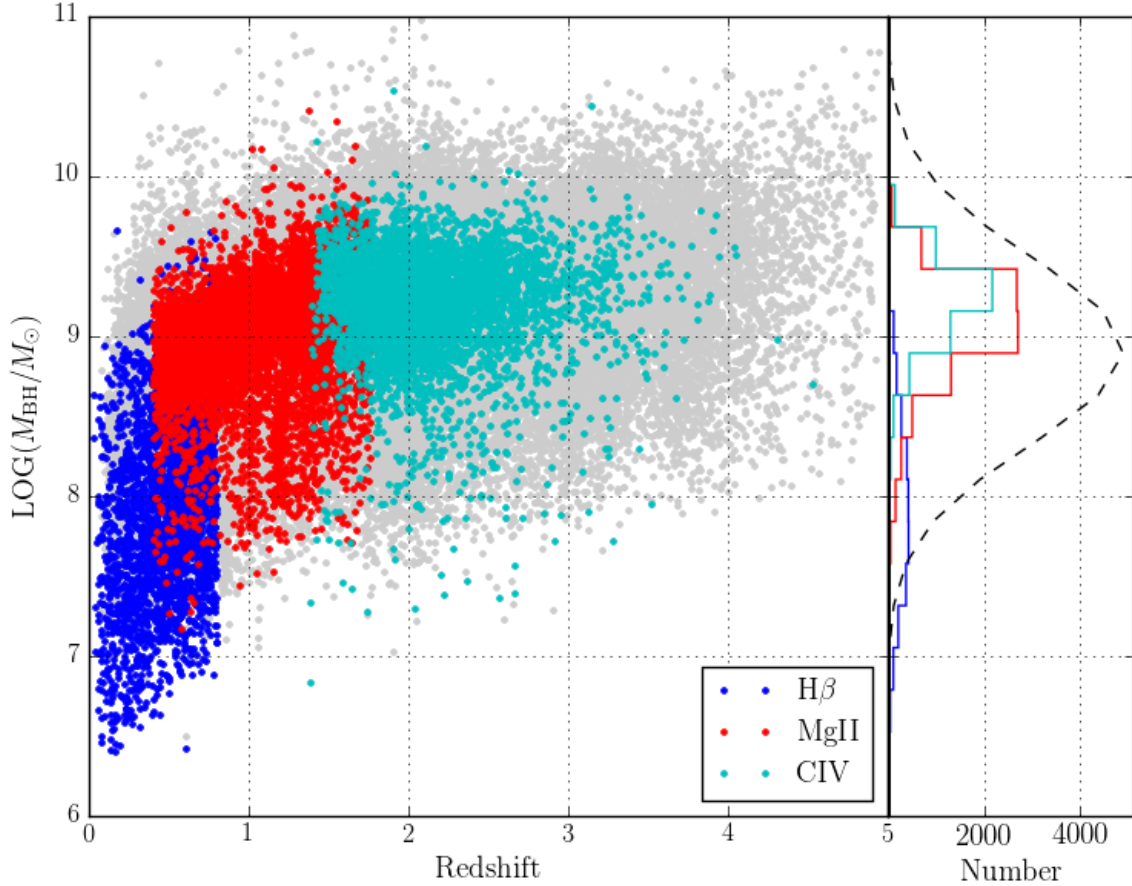


Fig. 12.— The left panel is the black hole mass distribution along the redshift. The grey dots are quasars from SDSS DR7 (Shen et al. 2011). The blue dots are LAMOST quasars with H β deduced black hole mass. The red dots are LAMOST quasars with MgII deduced black hole mass. The cyan dots are LAMOST quasars with CIV deduced black hole mass. It is clear that LAMOST quasars occupy the same black hole mass space as SDSS DR7 quasars. The black mass estimate in this work is reasonable. The right panel shows the histograms of BH masses deduced by H β (in blue), MgII (in red) and CIV (in cyan). The black dashed line is the distribution of the BH masses for the entire DR2 and 3 quasars.

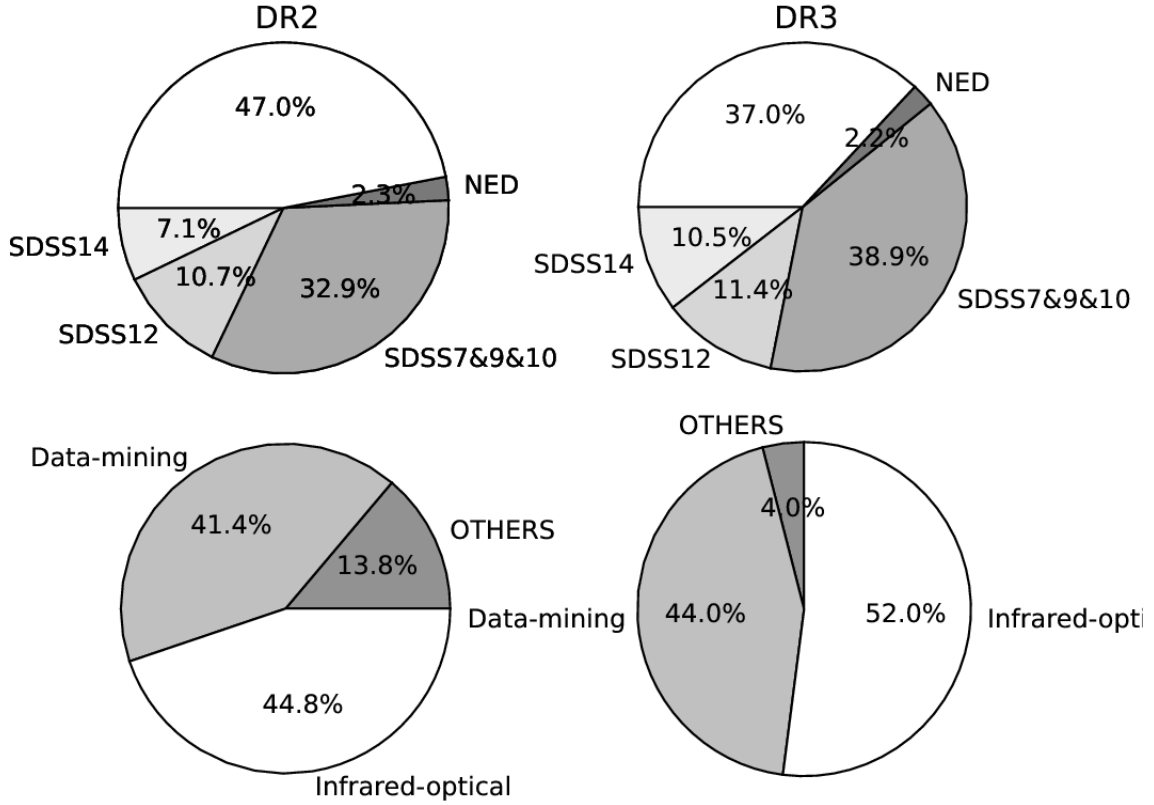


Fig. 13.— Sources of the quasar candidates. The top two pie plots are results from cross-matching SDSS quasars with LAMOST quasars. The grey areas are quasars reported in SDSS and NED. The white region is for quasars not reported in SDSS nor in NED. Over all, about 40% of quasars are not reported by SDSS. It indicates that LAMOST Quasar Survey provides a great supplement to low-to-moderate redshift quasar survey. The bottom two pie plots are sources of LAMOST quasar candidates. The white region is for quasars selected by infrared-optical colour. The light-grey area is for quasars selected by data-mining. The dark-grey area is for objects that not selected as quasar candidates, but are confirmed as quasars. It shows that infrared-optical colour selection results more quasars than any other selection methods.

Table 2:: The LAMOST quasar survey DR2 and 3 quasar
catalog: table description

Column	Name	Format	Description
1	OBSID	STRING	unique object id in LAMOST database
2	DESIGNATION	STRING	$hhmmss.ss + ddmms.s$ (J2000.0)
3	RA	DOUBLE	Right ascension in decimal degrees (J2000.)
4	DEC	DOUBLE	Declination in decimal degrees (J2000.0)
5	PLANID	STRING	spectroscopic plan identification
6	SPID	STRING	spectrograph identification
7	FIBERID	STRING	fibre number of the spectrum
8	MJD	STRING	MJD of the spectroscopic observation
9	SOURCE_FLAG	LONG	sources of quasar candidates
10	M_i	DOUBLE	absolute i -band magnitude with K -correction to $z = 2$ follows Richards et al. (2006)
11	CLASS_VI	STRING	classification given by visual inspection
12	CLASS_FLAG	SHORT	classification flag
13	Z_PIPELINE	DOUBLE	redshift given by LAMOST pipeline

14	Z_VI	DOUBLE	redshift given by visual inspection
15	Z_FLAG	SHORT	redshift quality flag
16	SNR_SPEC	DOUBLE	Median S/N per pixel of the spectrum
17	FWHM_BROAD_HA	DOUBLE	FWHM of broad H α in km s ⁻¹
18	EW_BROAD_HA	DOUBLE	rest-frame equivalent width of broad H α in Å
19	FWHM_NARROW_HA	DOUBLE	FWHM of narrow H α in km s ⁻¹
20	EW_NARROW_HA	DOUBLE	rest-frame equivalent width of narrow H α in Å
21	EW_NII_6585	DOUBLE	rest-frame equivalent width of [N II]6584 in Å
22	EW_SII_6718	DOUBLE	rest-frame equivalent width of [S II]6718 in Å
23	EW_SII_6732	DOUBLE	rest -frame equivalent width of [S II]6732 in Å
24	EW_FE_HA	DOUBLE	rest -frame equivalent width of Fe within 6000-6500 Å in Å
25	LINE_NPIX_HA	LONG	number of good pixels at the rest-frame 6400-6765 Å
26	LINE_MED_SN_HA	DOUBLE	median S/N per pixel at the rest-frame 6400-6765 Å
27	LINE_REDCHI2_HA	DOUBLE	reduced χ^2 of H α emission line fit
28	LINE_FLAG_HA	SHORT	quality flag of H α fitting
29	FWHM_BROAD_HB	DOUBLE	FWHM of broad H β in km s ⁻¹

30	EW_BROAD_HB	DOUBLE	rest-frame equivalent width of broad H β in \AA
31	FWHM_NARROW_HB	DOUBLE	FWHM of narrow H β in km s^{-1}
32	EW_NARROW_HB	DOUBLE	rest-frame equivalent width of narrow H β in \AA
33	EW_OIII_4959	DOUBLE	rest-frame equivalent width of [O III]4959 in \AA
34	EW_OIII_5007	DOUBLE	rest-frame equivalent width of [O III]5007 in \AA
35	EW_FE_HB	DOUBLE	rest-frame equivalent width of Fe within 4435-4685 \AA in \AA
36	LINE_NPIX_HB	LONG	number of good pixels at the rest-frame 4750-4950 \AA
37	LINE_MED_SN_HB	DOUBLE	median S/N per pixel at the rest-frame 4750-4950 \AA
38	LINE_REDCHI2_HB	DOUBLE	reduced χ^2 of H β emission line fit
39	LINE_FLAG_HB	SHORT	quality flag of H β fitting
40	FWHM_BROAD_MGII_2796	DOUBLE	FWHM of the broad MgII 2796 in km s^{-1}
41	EW_BROAD_MGII_2796	DOUBLE	rest-frame equivalent width of the broad MgII 2796 in \AA
42	FWHM_NARROW_MGII_2796	DOUBLE	FWHM of the narrow MgII 2796 in km s^{-1}
43	EW_NARROW_MGII_2796	DOUBLE	rest-frame equivalent width of the narrow MgII 2796 in \AA

44	FWHM_BROAD_MGII	DOUBLE	FWHM of the whole broad MgII in km s^{-1}
45	EW_BROAD_MGII	DOUBLE	rest-frame equivalent width of the whole broad MgII in \AA
46	FWHM_MGII	DOUBLE	FWHM of the whole MgII emis- sion line in km s^{-1}
47	EW_MGII	DOUBLE	rest-frame equivalent width of the whole MgII in \AA
48	EW_FE_MGII	DOUBLE	rest-frame equivalent width of Fe within 2200-3090 \AA
49	LINE_NPIX_MGII	LONG	number of good pixels at the rest- frame 2700-2900 \AA
50	LINE_MED_SN_MGII	DOUBLE	median S/N per pixel at the rest- frame 2700-2900 \AA
51	LINE_REDCHI2_MGII	DOUBLE	reduced χ^2 of MgII emission line fit
52	LINE_FLAG_MGII	SHORT	quality flag of MgII fitting
53	FWHM_BROAD_CIV	DOUBLE	FWHM of the broad CIV in km s^{-1}
54	EW_BROAD_CIV	DOUBLE	rest frame equivalent width of the broad CIV in \AA
55	FWHM_NARROW_CIV	DOUBLE	FWHM of the narrow CIV in km s^{-1}
56	EW_NARROW_CIV	DOUBLE	rest frame equivalent width of the narrow CIV in \AA

57	FWHM_CIV	DOUBLE	FWHM of the whole CIV in km s ⁻¹
58	EW_CIV	DOUBLE	rest-frame equivalent width of the whole CIV in Å
59	LINE_NPIX_CIV	LONG	number of good pixels at the rest- frame 1500-1600 Å
60	LINE_MED_SN_CIV	DOUBLE	median S/N per pixel at the rest- frame 1500-1600 Å
61	LINE_REDCHI2_CIV	DOUBLE	reduced χ^2 of CIV emission line fit
62	LINE_FLAG_CIV	SHORT	quality flag of CIV fitting
63	ALPHA1	DOUBLE	wavelength power-law index from 1300 to 4661 Å
64	ALPHA2	DOUBLE	wavelength power-law index from 4661 Å towards the red end of the spectrum
65	MODEL_PHOT_CHI2	DOUBLE	reduced chi-square of continuum fitting
66	CONT_FLAG	SHORT	quality flag of continuum fitting
67	LOGL1350	DOULBE	monochromatic luminosity at 1350 Å in units of erg/s
68	LOGL1350_ERR	DOUBLE	error of LOGL1350 in units of erg/s
69	LOGL3000	DOUBLE	monochromatic luminosity at 3000 Å in units of erg/s
70	LOGL3000_ERR	DOUBLE	error of LOGL3000 in units of erg/s

71	LOGL5100	DOUBLE	monochromatic luminosity at 5100 Å in units of erg/s
72	LOGL5100_ERR	DOUBLE	error of LOGL5100 in units of erg/s
73	LOGMBH_HB	DOUBLE	virial BH mass based on H β in units of M_{\odot}
74	LOGMBH_ERR_HB	DOUBLE	error of LOGMBH_HB in units of M_{\odot}
75	LOGMBH_HB_FLAG	SHORT	reliability of LOGMBH_HB
76	LOGMBH_MGII	DOUBLE	virial BH mass based on MgII in units of M_{\odot}
77	LOGMBH_ERR_MGII	DOUBLE	error of LOGMBH_MGII in units of M_{\odot}
78	LOGMBH_MGII_FLAG	SHORT	reliability of LOGMBH_MGII
79	LOGMBH_CIV	DOUBLE	virial BH mass based on CIV in units of M_{\odot}
80	LOGMBH_ERR_CIV	DOUBLE	error of LOGMBH_CIV in units of M_{\odot}
81	LOGMBH_CIV_FLAG	SHORT	reliability of LOGMBH_CIV